

Supplementary Information

SANS and rheology of elongated SDS-DDAO mixed micelles near the phase boundary

Luis M. G. Torquato^a, Gunjan Tyagi^a, Zain Ahmad^a, Liva Donina^a, Najet Mahmoudi^b, Rebecca Fong^c, Paul F. Luckham^a, and João T. Cabral^{a,*}

^a Department of Chemical Engineering, Imperial College London, London, SW7 2AZ

^b ISIS Neutron and Muon Source, Rutherford Appleton Laboratory, Didcot, OX11 0QX, UK.

^c Procter & Gamble, Newcastle Innovation Centre, Newcastle-Upon-Tyne NE12 9TS, United Kingdom

* j.cabral@imperial.ac.uk

1 Composition phase and optical birefringence

Figure S1 establishes that the concentrations (300-500 mM) and SDS:DDAO ratios (0-1) investigated fall within the micellar range. Employing cross-polarised microscopy at a fixed DDAO mol ratio of 70% (exhibiting the highest η_0) and increasing concentration from 500-600 mM, we find that 500 mM solution explored in this work is still in the micellar phase and thus the increase in viscosity must be related to changes in the micellar structure and interactions. At 575 mM, we begin to observe areas of 'streaming' birefringence in the samples as described by Weers *et al.* for a similar system of SDS-TDAO,¹ which span the whole solution at 600 mM, indicative of a mixed micellar-hexagonal phase and hexagonal phase respectively.

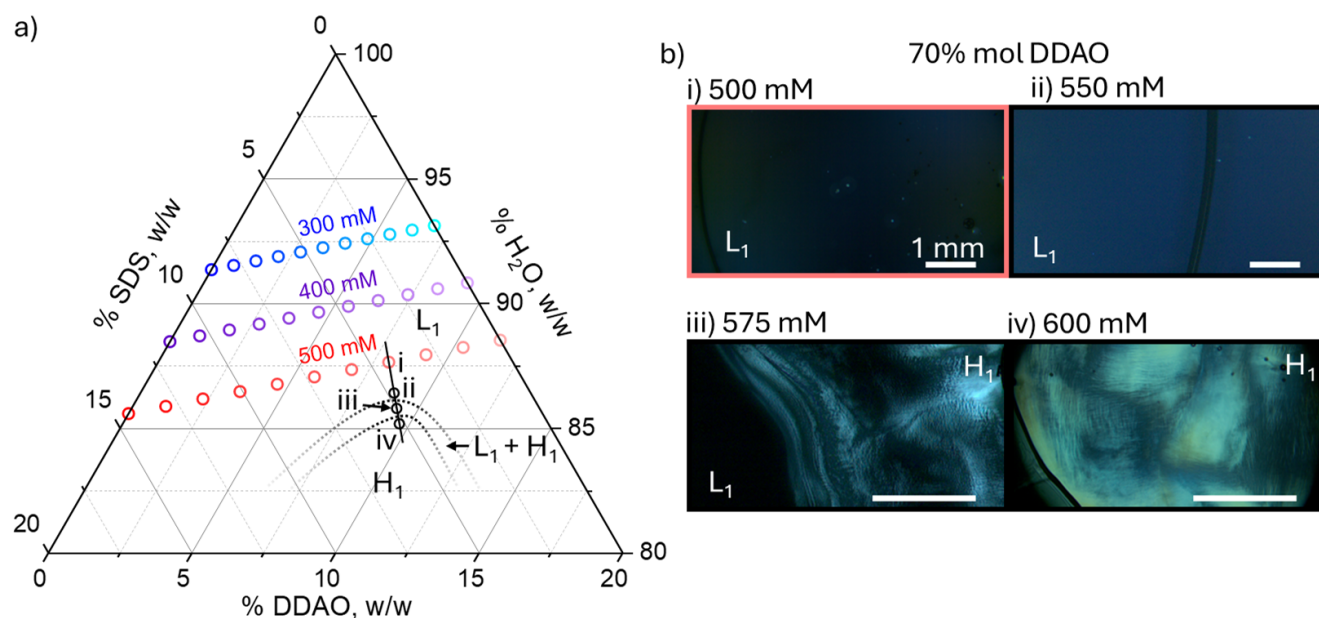


Figure S1. a) Reproduced ternary map of compositions investigated by SANS and rheology measurements (in blue, purple, and red), with additional constant ratio (70% mol DDAO) compositions of increasing concentration (black points) investigated under cross-polarised microscopy to determine the approximate phase boundaries shown. b) Polarised optical microscopy images of compositions i-iv (500, 550, 575, and 600 mM, 70% mol DDAO) around the phase boundary between the micellar (L_1), mixed (L_1+H_1), and hexagonal (H_1) phases. All scale bars represent 1 mm.

2 Methodology: SANS Data Fitting

2.1 Parameters and approach

Following data processing in MANTID, our approach to SANS data fitting was as follows. To enable comparison between different scattering studies on SDS, DDAO and their mixtures at various concentrations and mixing ratios,²⁻⁵ we employed the canonical core-shell ellipsoid form factor and Hayter_MSA structure factor using the standard form of the scattering intensity (Eqn. 2 of the main paper). In order to reduce the number of fitting parameters, the SLD of the shell was initially fixed according to the SDS:DDAO stoichiometry, following the solute fractions of the SDS and DDAO solutions, estimated using the 'SLD Calculator' tool on SASView using the headgroups (SO_4Na) for SDS and ($\text{C}_2\text{H}_6\text{NO}$) for DDAO. The core (dodecane) SLD was also calculated and fixed to $-0.4905 \times 10^{-6} \text{ \AA}^{-2}$ in good agreement with previous studies,^{2,4,5} and the solvent (D_2O) was fixed to $6.34 \times 10^{-6} \text{ \AA}^{-2}$: these are shown in Fig. S2a.

Following this, estimate volume fractions (V_{frac}) were calculated using cmc values from our previous work,⁶ and assuming a density of 1.01 g cm^{-3} . These were initially fixed, and then allowed to fluctuate. The relative permittivity of the medium was set to 78.06,⁷ and our approach assumed no difference in the shell thickness at the equator and poles of the micelle ($AS_{\text{shell}} = 1$). With this, all other parameters were fitted: the background, B , shown in Fig. S2b (whose slight variation may be associated with the cmc depression in mixed SDS-DDAO) and coherent contributions; micelle core equatorial radius, R_e ; core aspect ratio, $AR = R_p/R_e$, where R_p is the core polar radius; shell thickness, R_{shell} ; the effective radius used to calculate the structure factor, R_{eff} ; volume fraction, V_{frac} , and the micellar charge, Q_{mic} , all reported with the goodness of fit, χ^2 , in Table S1. Allowing the headgroup SLDs to vary within the limits of the pure surfactants did not meaningfully impact the fitting outcomes. During the fitting procedure, the polydispersity in the radii of the ellipsoid were adjusted to optimise the fits simultaneously. We found that fixing the $PD = \sigma / \langle R_e \rangle$, where σ is the standard deviation of the Gaussian distribution, and the brackets represent the mean, for the equatorial radius at 0.3 gave the best fits for all profiles.

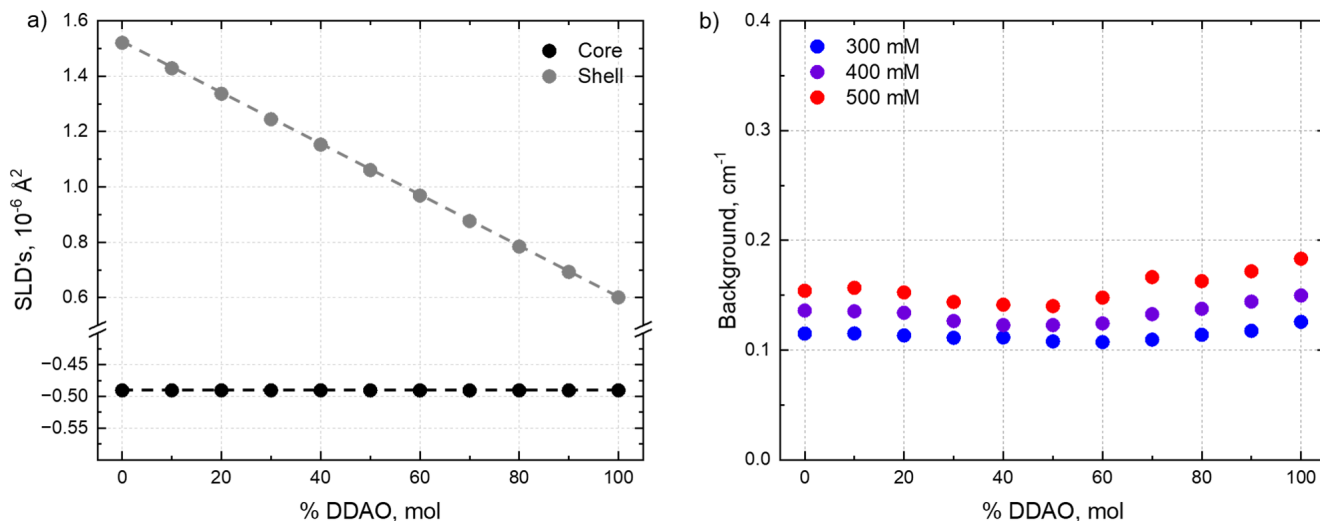


Figure S2. a) The scattering length densities (SLDs) for the core (black) and shell (grey) fixed for the SANS data fitting. b) The change in the fitted backgrounds with mol% DDAO for the 300 mM (blue), 400 mM (purple), and 500 mM (red) SDS-DDAO systems investigated.

Table S1. SANS fitting parameters obtained with SASView for all concentration series in this work. C_T is the total surfactant concentration (SDS and DDAO), B is the scattering background, R_e is the equatorial core radius of the prolate micelles, AR is the aspect ratio of the core radii (R_p/R_e) with R_p being the polar core radius, R_{Shell} is the shell thickness, R_{Eff} is the effective radius used to compute the structure factor, V_{Frac} is the volume fraction, Q_{Mic} is the micellar charge, and χ^2 is the goodness of fit estimated in SASView.

C_T , mM	%DDAO, mol	B , cm^{-1}	R_e , Å	AR	R_{Shell} , Å	R_{Eff} , Å	V_{Frac}	Q_{Mic} , e	χ^2
300	0	0.115	16.5	1.18	1.99	23.0	0.100	39.4	10.6
	10	0.115	16.0	1.43	2.50	24.3	0.103	38.8	11.3
	20	0.113	16.1	1.67	2.64	25.5	0.103	39.5	17.0
	30	0.111	16.0	2.04	2.97	27.0	0.105	38.3	28.2
	40	0.112	16.1	3.64	2.81	29.1	0.108	35.9	25.2
	50	0.108	16.1	5.10	2.89	31.1	0.105	34.2	13.4
	60	0.107	16.0	5.37	3.04	32.4	0.098	34.2	15.8
	70	0.109	15.8	4.67	3.37	34.5	0.104	40.5	74.3
	80	0.114	15.7	4.26	3.12	33.7	0.106	34.0	55.6
	90	0.118	15.6	2.63	2.39	30.3	0.101	13.1	33.7
	100	0.126	15.7	1.18	2.66	25.8	0.098	-	10.4
400	0	0.136	16.7	1.28	1.61	23.3	0.132	41.2	16.8
	10	0.135	16.3	1.55	2.20	24.7	0.136	39.5	22.0
	20	0.134	16.3	1.73	2.39	25.6	0.133	39.0	25.2
	30	0.126	16.3	1.67	2.32	25.3	0.120	40.2	22.2
	40	0.123	16.3	1.69	2.32	25.4	0.112	40.1	21.3
	50	0.123	16.3	4.08	2.58	29.5	0.122	34.7	9.56
	60	0.124	16.2	4.49	3.02	32.8	0.125	38.3	30.8
	70	0.133	16.1	3.90	3.42	33.5	0.140	41.2	57.5
	80	0.138	15.9	3.84	3.20	32.7	0.142	33.6	9.19
	90	0.144	15.8	2.94	2.24	30.0	0.137	16.0	22.0
	100	0.150	15.8	1.08	2.78	25.3	0.127	-	13.6
500	0	0.154	16.4	1.44	1.56	23.7	0.166	38.8	15.8
	10	0.157	16.1	1.77	2.23	25.2	0.175	36.1	17.1
	20	0.152	16.1	2.31	2.36	26.3	0.170	35.1	17.4
	30	0.144	16.1	2.38	2.38	26.5	0.155	35.8	17.7
	40	0.141	16.4	2.16	2.10	26.2	0.141	36.5	15.8
	50	0.140	16.1	3.81	2.64	28.6	0.145	33.4	9.83
	60	0.148	16.1	4.68	3.25	30.8	0.151	46.4	49.1
	70	0.166	15.9	5.08	3.92	32.1	0.183	63.5	52.7
	80	0.162	15.8	3.37	3.42	31.2	0.175	32.9	33.5
	90	0.172	15.7	2.75	2.22	28.6	0.168	15.1	23.7
	100	0.183	14.8	1.09	3.49	24.9	0.158	-	33.4

2.1.1 Form Factor

To critically assess the validity of using the core-shell ellipsoid form factor for the fits in this study, we examined a range of plausible models to fit the profile with the highest χ^2 , namely for 500 mM (70% mol DDAO), as shown in Fig. S3a in a log-log scale and b) in the Porod representations (after background subtraction).

We first show that SDS-DDAO micelles are better modelled by a prolate ellipsoidal shape as oppose to an oblate geometry, indicated by the tripling in χ^2 . Increasing the complexity of the model by the addition of a third major half-axis in the triaxial ellipsoid form factor, led to modest $\approx 10\%$ reduction in the χ^2 by using radii $R = 17, 26,$ and 78 \AA . Given the small change, we have opt to proceed with the prolate core-shell ellipsoid to keep the number of fitting parameters to a minimum, and for consistency with previous work by us and others.²⁻⁵

Finally, at the higher aspect ratios, we examined fitting to core-shell cylinder and bicelle form factors, which were found to decrease fit quality (to nearly double the χ^2) with respect to the prolate ellipsoid fit. From the Porod representation in Fig.S3b, we find small deviations around the second peak of the form factor (appearing as a shoulder in $I(q)$). Nevertheless, all fits but the bicelle form factor provide satisfactory fits to the mid-q region encompassing the first form and structure factor peaks to describe the changes and trends in the shape and interactions respectively of the SDS-DDAO micellar solutions with surfactant mixing. The prolate core-shell ellipsoid model provides overall the best description of the data (and lowest χ^2) including at the higher q values, and is therefore selected for the analysis presented in the main paper.

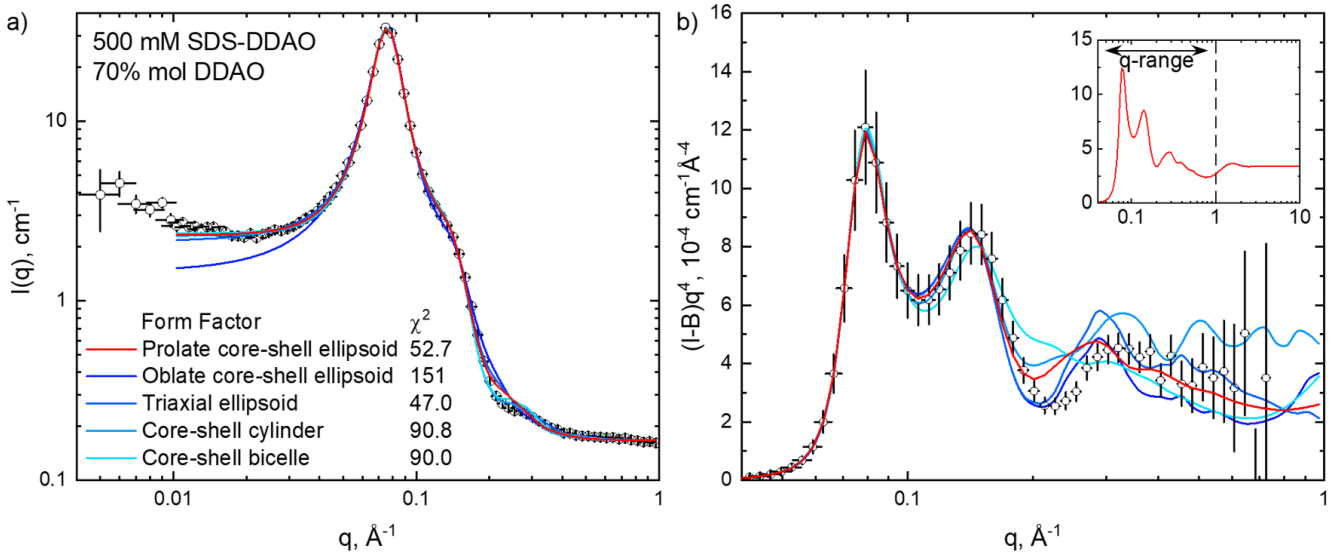


Figure S3. a) Examples fits (lines) to the 500 mM, 70% mol DDAO sample 1D scattering profile (points) using the Hayter_MSA structure factor and a range of form factors as shown along with their respective χ^2 . The red line fit is the fit used in this study for this sample while the blue lines represent similar form factor models trialed. b) Porod representation of (a). The inset is the prolate core-shell ellipsoid fit to a greater q -range than experimentally measured.

2.1.2 Non-spherical structure factor

The Hayter-Penfold mean spherical approximation (Hayter-MSA) structure factor model used in this work assumes the solution structure of charged, spherical macroions (size defined by the effective radius, R_{eff}) arises due to their interaction through a repulsive Coulomb potential, screened by the solvent and counterions in solution.^{9,10} For micelles with aspect ratios (AR) significantly deviating from 1 (sphere), we evaluated a model formulated by Kotlarchyk and Chen using a modified form of the scattering intensity:⁸

$$I(q) = kP(q)[1 + \beta(q)(S(q) - 1)] + B, \quad (1)$$

where $k = (N/V)V_p^2\Delta\rho^2$, with (N/V) the number density of scatters, V_p their volume, $\Delta\rho$ the scattering length density (SLD) difference between particle and solution, B is the scattering background, $P(q)$ the form factor of the scatters, $S(q)$ is their structure factor, and $\beta(q)$ is a q -dependent factor, taking values from 0 to 1, given by the ratio:⁸

$$\beta(q) = \frac{|\langle F(q) \rangle|^2}{\langle |F(q)|^2 \rangle}, \quad (2)$$

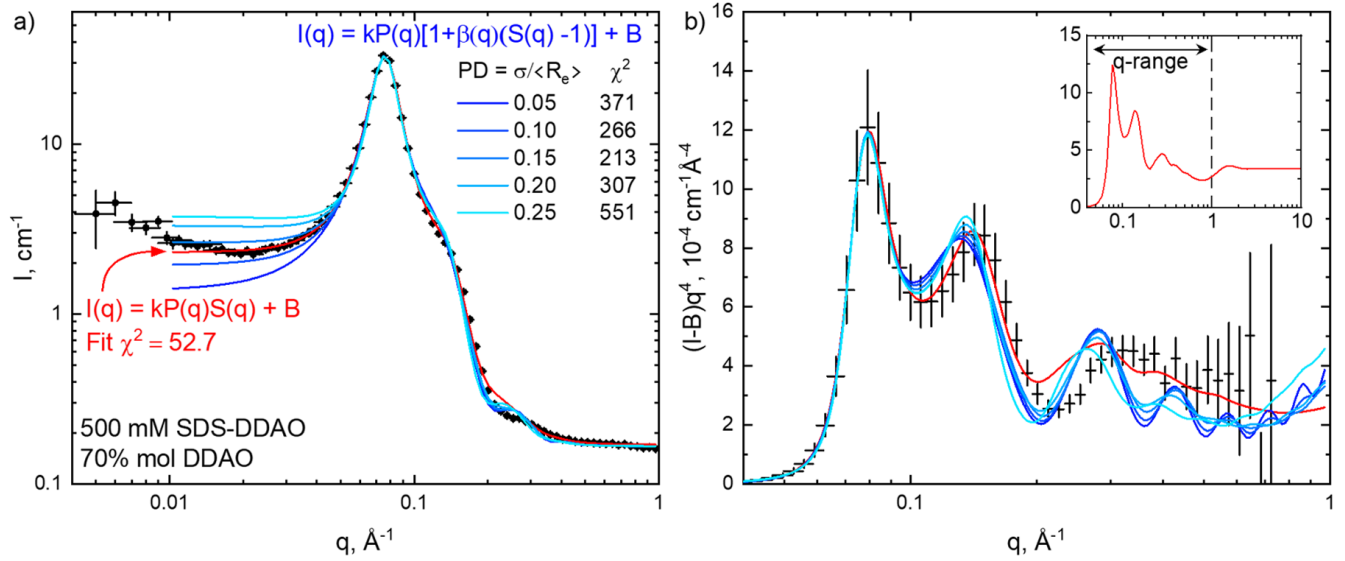


Figure S4. Examples fits (lines) of the radially averaged 1D scattering profile for the 500 mM, 70% mol DDAO sample data (points), with a prolate ellipsoid form factor and Hayter-MSA structure factor using the routine form of the scattering intensity (red), and the Kotlarchyk and Chen form⁸ (blue) with a range of polydispersity parameters ($PD = \sigma / \langle R_e \rangle$, where σ is the standard deviation, and $\langle R_e \rangle$ the mean of the Gaussian distribution of R_e), and their respective χ^2 . b) Porod representation of (a). The inset shows the fit using the routine form of the scattering intensity used in this work, for a greater q -range than experimentally measured.

where $P(q) = \langle |F(q)|^2 \rangle$, the vertical lines represent multiplying by the complex conjugate, and the angled brackets represent averaging over all particle sizes and orientations. Instead of formulating a new non-spherical structure factor model for charged non-spherical objects, Kotlarchyk and Chen showed that the dampening of the structure factor oscillations by this $\beta(q)$ factor yielded improved fits both polydisperse and non-spherical model systems.⁸ We illustrate the fitting results with the profile of highest χ^2 in the 500 mM series (70% mol DDAO), systematically changed the polydispersity parameter ($PD = \sigma / \langle R_e \rangle$) for the equatorial radius of the micelles (we found that polydispersity in the aspect ratio parameter had little effect on the fits) with σ being the standard deviation of the Gaussian distribution of radii, and $\langle R_e \rangle$ is the mean equatorial radius.

A summary of our findings is shown in Fig. S4, in both log-log and (background-subtracted) Porod representations, of the Hayter-MSA fit used in this work (in red) and the Kotlarchyk and Chen fits at varying PD , shown in blue. The dampening effect of the latter can be observed by the increase in intensity of the fits in the low- q region when increasing the standard deviation of the equatorial radius. The best fits using this model are obtained for $0.1 < PD < 0.15$, although this still leads to an approximate 4 fold increase in the χ^2 . We therefore opt to employ the canonical core-shell ellipsoidal form factor and spherical Hayter-MSA structure factor for all datasets, allowing for the effective radius R_{eff} to fit independently of the form factor radii (e.g., the equivalent radius $R_{eff} = R_{equiv} = (R_e^2 R_p)^{1/3}$). This procedure allowed us to model the structure factor of the highly ellipsoidal micelles with a spherical particle of radius R_{eff} that gives rise to the same structure factor. To check that this fitted parameter retained physical significance, we show that it scales well with form factor radii and equivalent radius, as shown in Fig. S5a, b, and c, respectively. The slightly greater variation in the equatorial radius away from the trend is attributed to the fitting error as the variation in values is small (~ 1.5 Å), across all concentrations and ratios.

Although this approach to the SANS data analysis yields parameters (e.g. R_{polar} and Q_{mic}) that vary expectedly (increase and remain constant respectively) with surfactant mixing ratio, and follow known behaviour when compared to previous works, the analysis remains an approach to the true system.^{2,3} Due to a high volume fraction and high aspect ratios especially for the 500 mM series in the range of 60-70% mol DDAO, the crowding of ellipsoids in the system may yield short-range strong correlations and organisation within the sample, in other words, a locally nematic but globally isotropic system. Therefore, an analysis of scattering data approaching the hexagonal phase should likely include a strong directional dependence of the structure factor of the micelles, $S(\vec{q})$, albeit possibly yielding an overall isotropic profile ('powder average') and structural coarsening or relaxation into a liquid crystalline phase.

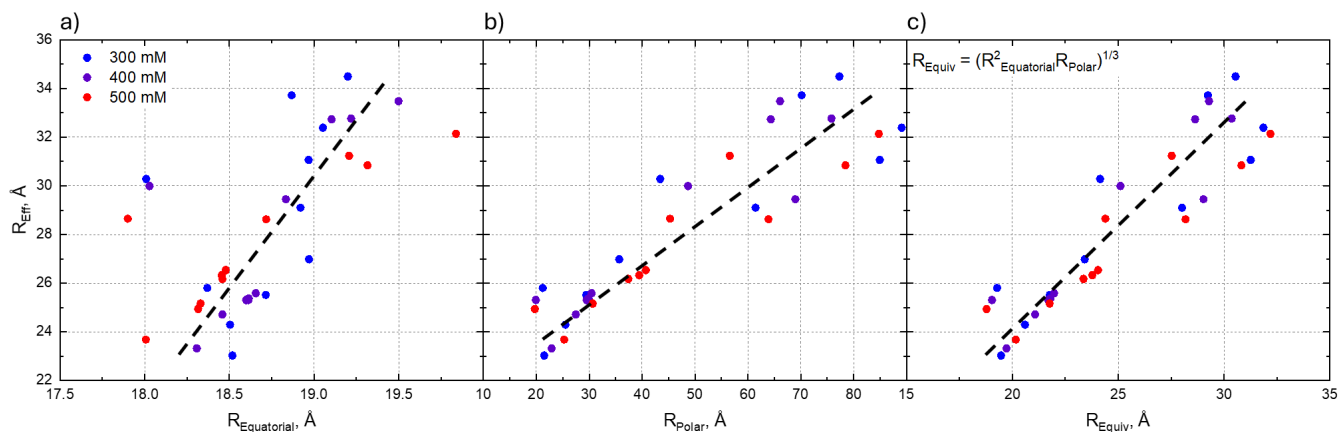


Figure S5. Correlation between the effective radius, R_{Eff} , used in calculating the structure factor and the (a) equatorial, $R_{Equatorial}$, (b) polar, R_{Polar} , and (c) equivalent, $R_{Equiv} = (R_{Equatorial}^2 R_{Polar})^{1/3}$ radii for 300 mM (blue), 400 mM (purple), and 500 mM (red) SDS-DDAO solutions of varying mol% DDAO ratios.

2.2 Porod representation of 300 mM data fits at varying stoichiometry

Figure S6 shows the Porod representation of our (background-subtracted) data and fits for a representative sample of the 300 mM data showing good agreement with measurement, within experimental uncertainty. Within this range, a q -independent plateau is not expected, as shown in inset, which is only recovered at even higher q .

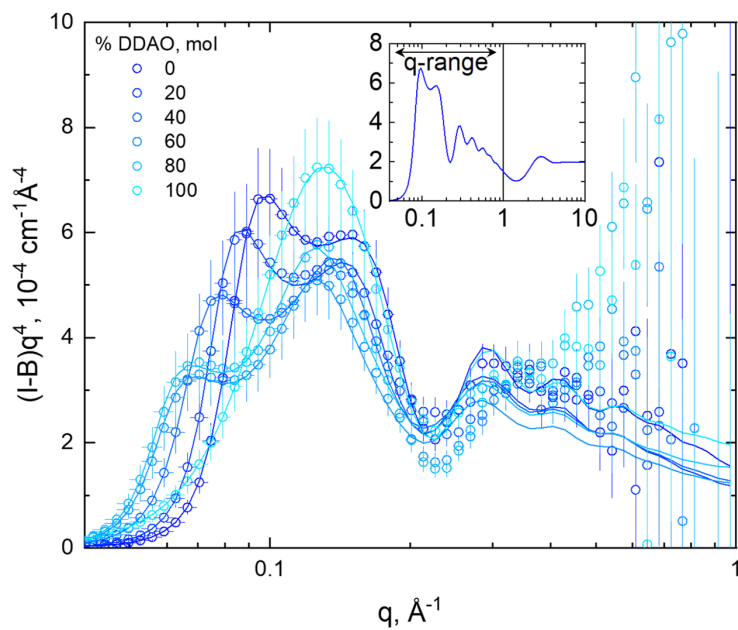


Figure S6. Porod representation of the fits and data (background-subtracted) for 300 mM solutions for selected ratios (%mol DDAO). The inset shows the 20% mol DDAO fit to a greater q -range than experimentally measured.

3 Rheology data for 300 mM and 400 mM SDS-DDAO solutions and concentration dependence

Figure S7 shows the data obtained from a shear rate sweep of a) 300 mM and b) 400 mM SDS-DDAO solutions of varying DDAO mol compositions. These data show a similar trend as that of the 500 mM set in the main paper: viscosity increases with DDAO addition up to a maximum at 80% and 70% mol DDAO for 300 mM and 400 mM solutions respectively followed by a decrease towards pure DDAO. Shear thinning behaviour is observed for mixing ratios towards the DDAO-rich stoichiometries in line with conclusions from the 500 mM data. Flow curves exhibiting this shear thinning behaviour were fit with the Carreau model (Eqn. 1 in the main paper) with parameters shown in Fig.S7, while other curves were fit with a straight line to extract the zero-shear viscosities η_0 used in the main paper.

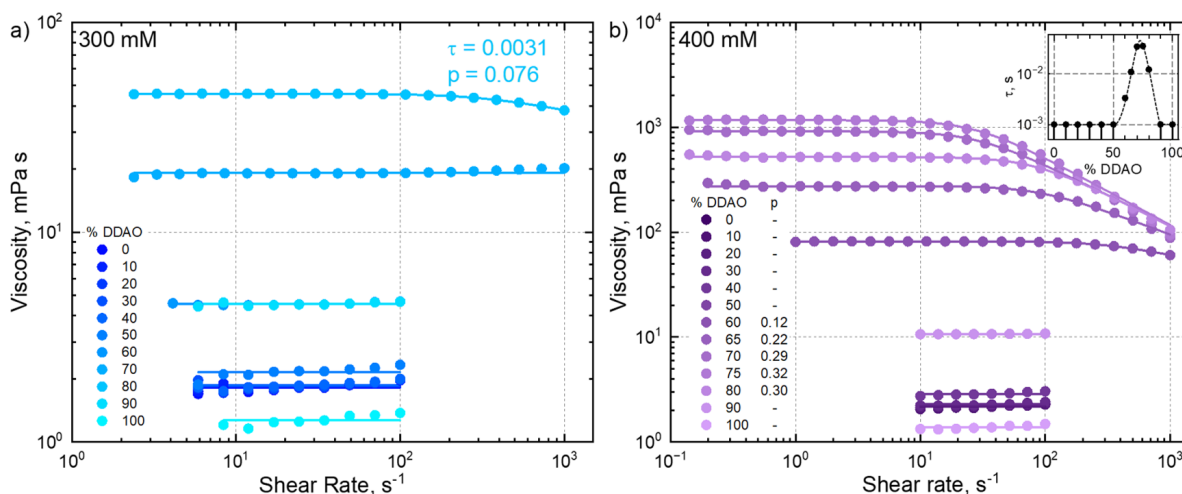


Figure S7. Shear rate sweeps of a) 300 mM and b) 400 mM solutions of SDS-DDAO for varying %mol DDAO. The lines are linear fits to the data with samples exhibiting shear thinning fit with the Carreau model. Parameters τ and p from the latter fit are shown, with the inset in (b) plotting the relaxation times for the 400 mM solutions. Additional % mol DDAO compositions were measured (65% and 75%) about the composition of highest viscosity.

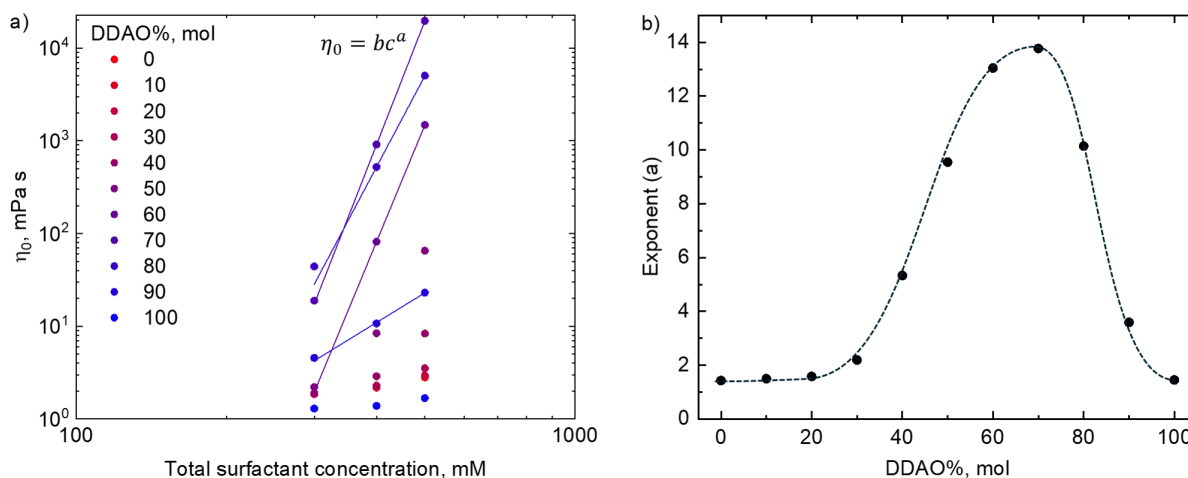


Figure S8. a) The viscosity of SDS-DDAO samples with concentration at fixed DDAO% mol ratios. Lines are select fits to $\eta_0 = bc^a$. b) The exponent, a , from fits in a) for the range of DDAO mol%. The dashed line is a guide to the eye.

Figure S8a shows the concentration dependence of the zero-shear viscosity for our systems. The data and fits show that the viscosity varies in accordance with the normal power law ($\eta_0 \propto C^a$), where C is the solution concentration and a is the power law exponent and is shown in Fig. S8b.

4 Micelle core and shell dimensions

A core-shell ellipsoid form factor was used in fitting SANS data of SDS-DDAO micelles. Figure S9a shows the fitted dimensions for the two major radii of the core, showing an increase with DDAO addition up to maximum at $\approx 60\text{-}70\%$ mol DDAO, and a decrease thereafter. As expected, these results follow those of the overall micellar dimensions shown in the main paper, as the shell thickness (Fig. S9b) is comparatively very small (as the data variations within the instrumental resolution).

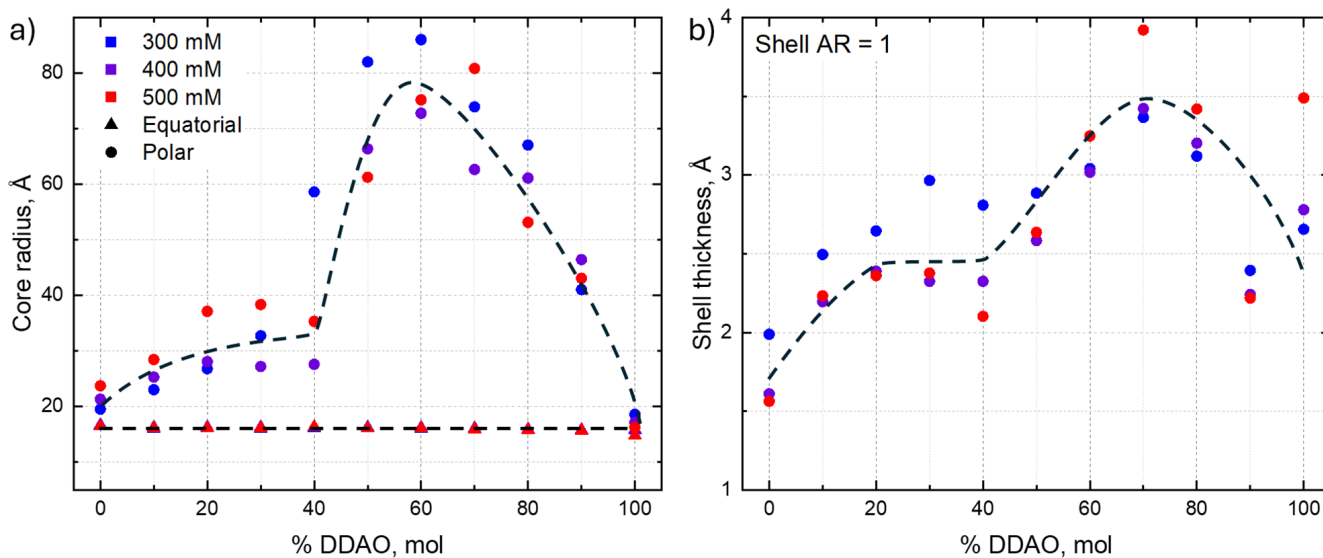


Figure S9. a) The equatorial, \triangle , and polar, \circ , core radii of micelles extracted from SANS fits in this work for 300 mM (blue), 400 mM (purple), and 500 mM (red) total surfactant concentrations of varying %DDAO mol ratios. b) *Idem* for the shell thickness of micelles. Dashed lines represent a guide to the eye of trends across all concentrations.

5 Monomer and surface charge

Figure S10 shows the (a) average charge per monomer in the micelle $\equiv Q_{Mic}/N_{Agg}$ and (b) the surface charge density of the micelle $\equiv Q_{Mic}/A_{Surface}$, where $A_{Surface}$ is the surface area of the prolate ellipsoid micelle. As the charge parameter is approximately constant with DDAO addition up to $\sim 80\%$ mol DDAO (with the exception of the increase at 60% and 70% mol DDAO solutions at 500 mM), these charge parameters follow the inverse of the trend in polar radius. The overall decrease is attributed to the reduction in the fraction of SDS monomers with increasing DDAO mol% in the micelle, and thus a decrease in the major component contributing to the electric double-layer interaction (anionic SDS, where DDAO is amphoteric, either non-ionic or cationic dependent on the local pH environment).¹¹

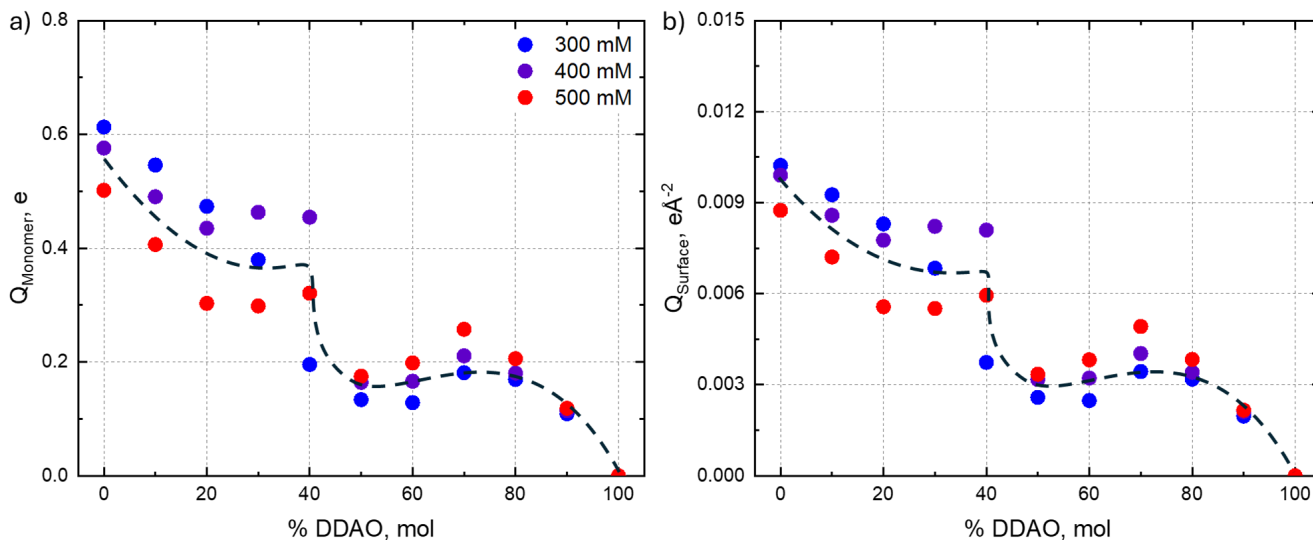


Figure S10. (a) Average charge of monomers that constitute the micelles, $Q_{Monomer} = Q_{Mic}/N_{Agg}$, and (b) the surface charge density of the micelle, $Q_{Surface} = Q_{Mic}/A_{Surface}$, for SDS-DDAO solutions of 300 mM (blue), 400 mM (purple), 500 mM (red) total concentrations and varying mol% DDAO ratios. Dashed lines are guides to the eye across all concentrations.

6 Scattering anisotropy of elongated micellar solutions

Due to the relative large aspect ratio of micelles, solution viscosity, and sudden peak in the charge, specifically for 500 mM solutions, around 60-70% mol DDAO, 2D SANS spectra were analysed as shown in Fig. S11a. We follow a concentration series along the ratios of maximum polar radius, 60% for 300 mM and 400 mM, and 70% for 500 mM (i-iii), and four ratios for the 500 mM solutions, 50-80% mol DDAO (iv, v, iii, vi). We select a narrow q -range (of three data points) centred at the peak intensity of the respective scattering profiles, as illustrated in Fig. S11b. The intensity scale of the 2D spectra was adjusted to a range of 8 cm^{-1} for all scattering patterns to better visualise the scattering anisotropy around the peak (illustrated with the data for composition iii) at the bottom of Fig. S11b) which becomes apparent at 500 mM and 60-70% mol DDAO ratios, coinciding with the peak in micellar charge. Azimuthal analysis (Fig. S11c) shows a small scattering intensity variation of approximately $\pm 2.5 \text{ cm}^{-1}$ at those ratios corresponding to $\lesssim 5\%$ fluctuation in the scattering intensity relative to the max intensity of the azimuthally averaged 1D profiles.

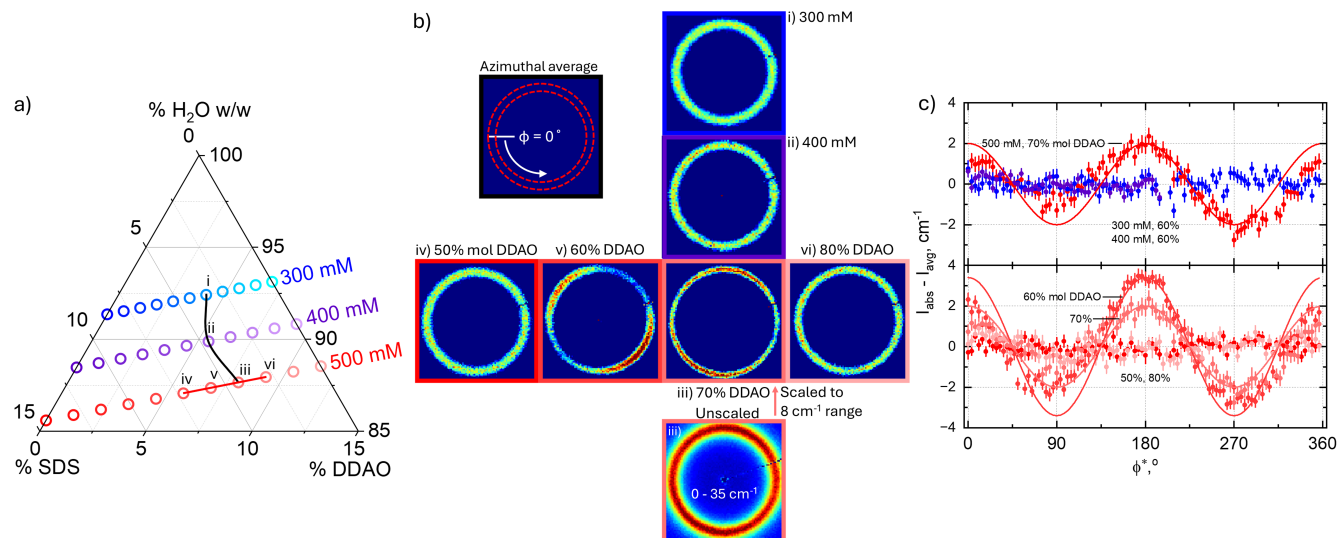


Figure S11. a) Ternary map (% w/w) highlighting compositions i-vi depicted in the azimuthal analysis of 2D scattering profiles. Compositions i, ii, and iii follow the ratios of maximum micelle polar radius. b) Schematic of azimuthal averaging and reduced 2D scattering patterns for solutions i-vi. The region of analysis was defined by a narrow q interval around the scattering intensity peak in Fig. 3 of the main paper. To emphasise the slight anisotropy, the colour map was re-scaled to an 8 cm^{-1} interval centred at the peak intensity. c) Variation of azimuthal scattering intensity (\circ), subtracted by the average intensity, as a function of azimuthal angle for i-iii (top) and iii-vi (bottom). Lines represent a sinusoidal fit to the data ($a \cdot \sin(\phi^*) + b$) where $\phi^* = \phi_{\text{abs}} - \phi_{\text{peak}}$ is the rescaled azimuthal angle to enable comparison of datasets.

Scattering anisotropy is expected for wormlike micelles (e.g., erucyl bis(hydroxyethyl) methylammonium chloride (EHAC) in KCl¹²) and for surfactant systems (e.g., vinyl alkyl quaternary ammonium bromide and sodium salicylate¹³) under shear. In our experiments, we expect this slight anisotropy to be caused either by elongated, charged micelle alignment in viscous solutions, upon loading into SANS quartz cells, that does not relax (within $> 1\text{h}$) prior to measurement, or induced alignment near cell walls (e.g.,¹⁴). Microfluidic approaches can quantify flow response and alignment, and have been coupled with SANS and SAXS,¹⁵⁻²⁰ and a range of analytical techniques. To elucidate the anisotropy in our measurements, we investigated the relaxation of this shear-induced alignment in a contraction microfluidic channel by cross-polarised microscopy. Fig. S12 shows the mean intensity averaged over the wide channel section, along with the flow rate programme used in the inset (a pulse of 1 mL min^{-1} for 12 s from $t = 0 \text{ s}$) and the dimensions of the channel for the %DDAO mol ratios of greatest aspect ratio for the 300 mM and 500 mM concentration (60% and 70% respectively). The 300 mM solution shows no change in the mean intensity before, during or after the flow pulse suggesting no induced alignment during the loading of these samples. For the 500 mM solution, as suspected, we observe flow induced birefringence as can be seen by the micrographs in Fig. S12b, and its decay upon cessation of flow. Fitting this drop with a double exponential decay function gives a 1.0 s timescale (in agreement with the Carreau relaxation time) and a longer decay. We therefore infer that while the bulk alignment in our SANS measurements has relaxed rapidly, the residual anisotropy observed is likely due to experimental cell wall affinity which persists over longer times.

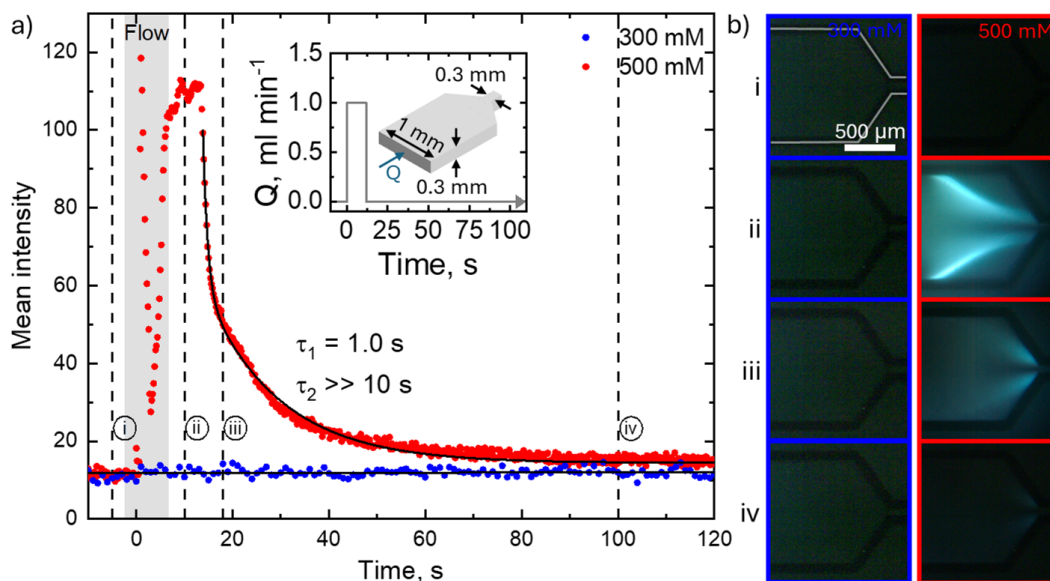


Figure S12. a) Evolution of mean cross-polarised optical intensity following a flow pulse, measured within the illustrated microfluidic channel with solutions of 300 mM, 60% mol DDAO (blue) and 500 mM, 70% mol DDAO (red) SDS-DDAO. Time $t = 0$ is defined at the start of the 12 s flow pulse (shown in inset) and the solid lines represent a double exponential decay (for 500 mM) and straight line (for 300 mM) fit to the data. b) Micrographs of the cross-polarised sequence at the indicated times in (a), namely, i) before flow (-5 s), ii) during flow (10 s), iii) just after flow (18 s), and near the plateau in intensity (100 s) for the 300 mM (blue) and 500 mM (red) systems. All micrographs have the same scale bar, the channel is outlined in white in the first micrograph, and the brightness threshold for the 300 mM micrographs was adjusted (increased by a factor of 3) post-intensity analysis to better show the channel and absence of birefringence.

7 Structure factors from fits of 300 mM and 400 mM data

Structure factors were also extracted from $I(q)$ fits to our 300 mM and 400 mM data series for interpretation in connection to the viscosity of solutions, as shown in Fig. S13a and b respectively. The profiles were stacked and offset by +1 for clarity, for all DDAO ratios investigated. Here, the parameter of interest is the position of the maximum of $S(q)$ function, assigned as q_{peak} , and indicated with the dashed line showing a shift to lower q (or larger lengthscales) with DDAO addition up to 70% and 60% mol DDAO, before shifting to higher q , shorter lengthscales for the 300 mM and 400 mM series respectively.

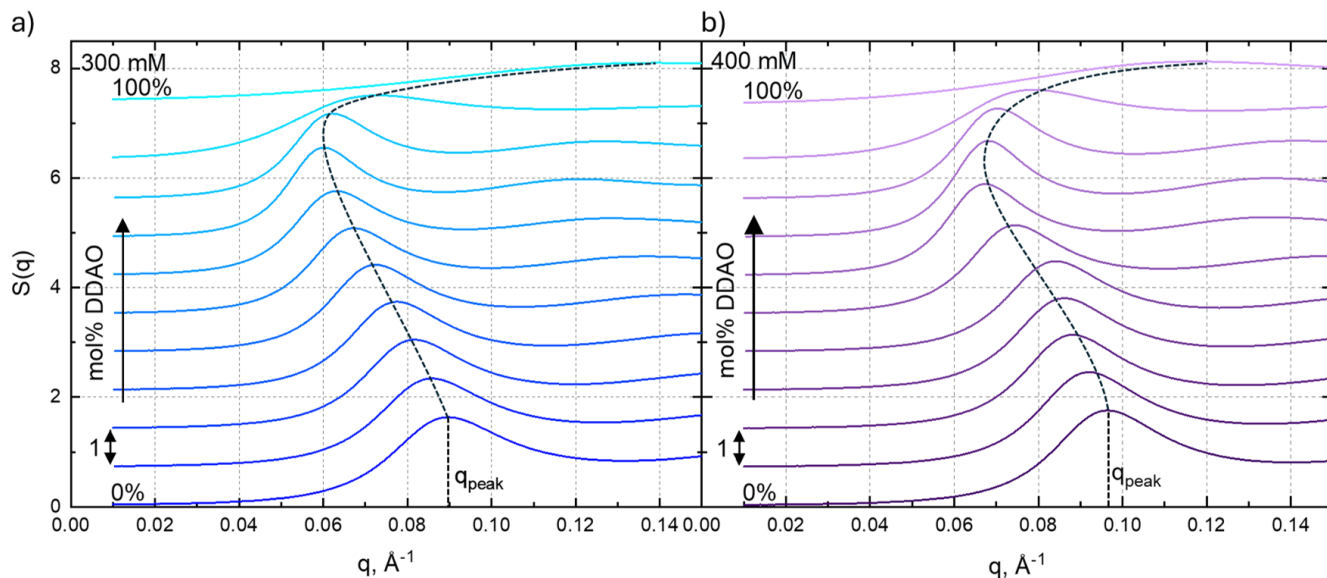


Figure S13. Structure factors from fitted models of SANS data for the (a) 300 mM and (b) 400 mM surfactant solutions of increasing mol% DDAO in steps of 10% from bottom to top. Curves are stacked and separated by a step of 1, and the dashed line shows a guide to the eye of the maximum (first peak) in $S(q)$, and the corresponding q value defined as q_{peak} .

8 Geometric correlations between viscosity and R_{Polar}

In the main paper, we observed a clear correlation between the viscosity of solution and the polar radius, and hence the volume, of micelles for the 500 mM systems (close to the H_1 phase). We have considered whether a better correlation could be obtained by considering restrictions to the rotational motion of elongated micelles, as illustrated in Fig. S14. We thus define the volume, V_{Rot} , that would be swept by a rotating prolate ellipsoid micelle (shown in orange), such that:

$$V_{Rot} = \frac{4}{3}\pi R_{Polar}^3. \quad (3)$$

which is illustrated as a red sphere in Fig. S14a. The volume fraction, $V_{Frac,Rot}^*$, of such sphere was then calculated to estimate the degree of overlap of these volumes, using:

$$V_{Frac,Rot}^* = \frac{V_{Frac}}{V_{Mic}} V_{Rot}, \quad (4)$$

where, V_{Frac} is the volume fraction from the SANS fits and V_{Mic} is the micelle volume, calculated from their polar and equatorial radii. Figure S14a shows the dependence of this effective volume fraction with DDAO mol ratio. These calculated effective volume fractions show an increase with DDAO addition up to 70% mol DDAO before decreasing, where between 50% < %DDAO < 90% the volume fraction is above 74%, the approximate packing fraction of close packed spheres. For solutions in this range, the micelles could be expected to exhibit restrictions to rotational motion, i.e. some rotational motions would lead to collisions for static centres of mass. With the equatorial radius and volume fractions from SANS fits remaining approximately constant (such that, approximately, $V_{Frac,Rot}^* \propto R_{Polar}$) we observe a good exponential correlation between the zero-shear viscosity and $V_{Frac,Rot}^*$ as shown in Fig. S14b. However, this correlation is no better than that shown in Fig. 7 of the main paper, with $V_{Micelle}$, and neither argument considers micellar interactions, thus relating only solution viscosity to the volume of a single micelle, at fixed overall surfactant concentration.

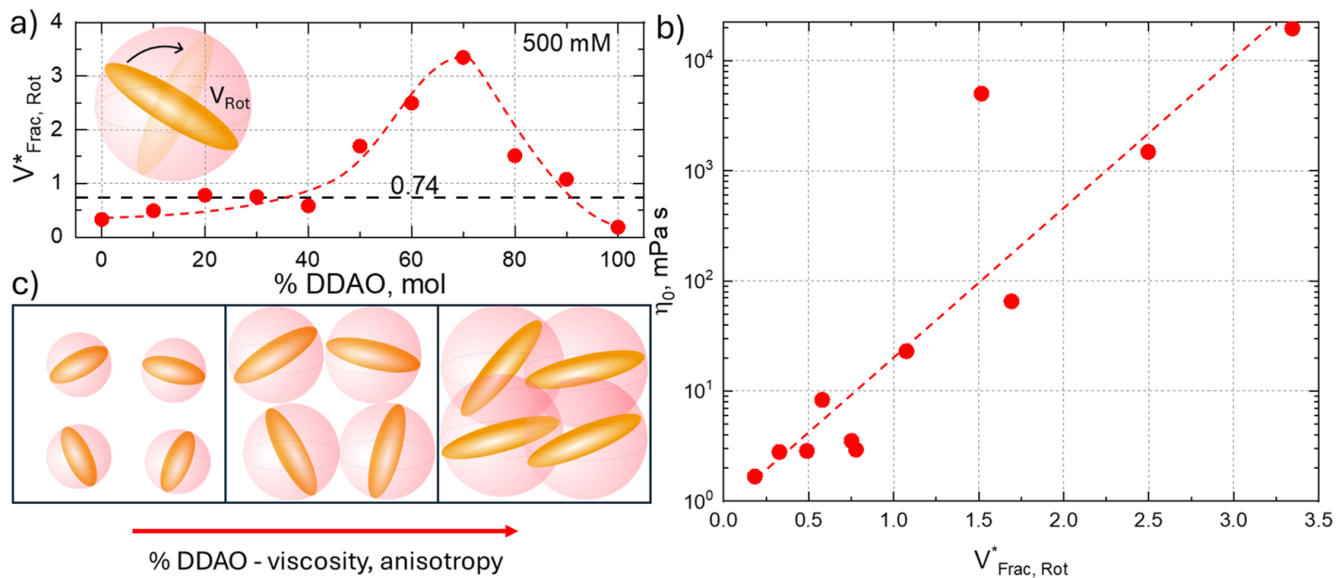


Figure S14. a) The effective volume fraction of the sphere containing all possible rotational perturbations of the micelle at different DDAO mol ratios for 500 mM solutions. These were calculated with parameters from fitting SANS data and using Eqn. 3 and Eqn. 4. b) The increase in zero-shear viscosity of solutions with the effective volume fraction of the rotational sphere. The dashed line is a guide to the eye. c) Physical illustration of spacing, orientation, and overlap of rotational volumes of micelles and the rotation spheres with increasing DDAO ratio up to the maximum at 70% mol DDAO.

References

1. Weers, J., Rathman, J. & Scheuing, D. Structure/performance relationships in long chain dimethylamine oxide/sodium dodecylsulfate surfactant mixtures. *Colloid Polym. Sci.* **268**, 832–846 (1990).
2. Torquato, L. M. *et al.* Concentration dependent asymmetric synergy in sds-ddao mixed surfactant micelles. *Langmuir* **40**, 7433–7443 (2024).
3. Tyagi, G. *et al.* Solution structures of anionic–amphoteric surfactant mixtures near the two-phase region at fixed ph. *Langmuir* **38**, 7198–7207 (2022).
4. Hammouda, B. Temperature effect on the nanostructure of sds micelles in water. *J. Res. Natl. Inst. Standards Technol.* **118**, 151 (2013).
5. Khodaparast, S. *et al.* Pure and mixed aqueous micellar solutions of sodium dodecyl sulfate (sds) and dimethyldodecyl amine oxide (ddao): Role of temperature and composition. *J. Colloid Interface Sci.* **582**, 1116–1127 (2021).
6. Tyagi, G. *et al.* Tensiometry and ftir study of the synergy in mixed sds: Ddao surfactant solutions at varying ph. *Colloids Surfaces A: Physicochem. Eng. Aspects* **618**, 126414 (2021).
7. Vidulich, G. A., Evans, D. F. & Kay, R. L. The dielectric constant of water and heavy water between 0 and 40. degree. *The J. Phys. Chem.* **71**, 656–662 (1967).
8. Kotlarchyk, M. & Chen, S.-H. Analysis of small angle neutron scattering spectra from polydisperse interacting colloids. *The J. Chem. Phys.* **79**, 2461–2469 (1983).
9. Hayter, J. B. & Penfold, J. An analytic structure factor for macroion solutions. *Mol. Phys.* **42**, 109–118 (1981).
10. Hayter, J. & Hansen, J. A rescaled msa structure factor for dilute charged colloidal dispersions. *Mol. Phys* **46**, 651–656 (1982).
11. Soontravanich, S., Munoz, J. A., Scamehorn, J. F., Harwell, J. H. & Sabatini, D. A. Interaction between an anionic and an amphoteric surfactant. part i: Monomer–micelle equilibrium. *J. Surfactants Deterg.* **11**, 251–261 (2008).

12. Croce, V. *et al.* Giant micellar worms under shear: a rheological study using sans. *Langmuir* **21**, 6762–6768 (2005).
13. Lin, M. *et al.* A small angle neutron scattering study of worm-like micelles. *Phys. B: Condens. Matter* **213**, 613–615 (1995).
14. Wang, R., Ginzburg, V. V., Jiang, J. & Wang, Z.-G. Adsorption of a polyelectrolyte chain at dielectric surfaces: effects of surface charge distribution and relative dielectric permittivity. *Macromol.* **56**, 7653–7662 (2023).
15. Lopez, C. G., Watanabe, T., Martel, A., Porcar, L. & Cabral, J. T. Microfluidic-sans: flow processing of complex fluids. *Sci. reports* **5**, 1–7 (2015).
16. Martin, H. P. *et al.* Microfluidic processing of concentrated surfactant mixtures: online saxs, microscopy and rheology. *Soft Matter* **12**, 1750–1758 (2016).
17. Poulos, A. S. *et al.* Microfluidic saxs study of lamellar and multilamellar vesicle phases of linear sodium alkylbenzenesulfonate surfactant with intrinsic isomeric distribution. *Langmuir* **32**, 5852–5861 (2016).
18. Donina, L., Rafique, A., Khodaparast, S., Porcar, L. & Cabral, J. T. Lamellar-to-mlv transformation in sds/octanol/brine examined by microfluidic-sans and polarised microscopy. *Soft Matter* **17**, 10053–10062 (2021).
19. Fischer, J., Porcar, L., Cabral, J. T. & Sottmann, T. Shear-induced sponge-to-lamellar transition in bicontinuous microemulsions evidenced by microfluidic-sans. *J. colloid interface science* **635**, 588–597 (2023).
20. Torquato, L. M. *et al.* Microfluidic in-line dynamic light scattering with a commercial fibre optic system. *Lab on a Chip* **23**, 2540–2552 (2023).